Measurement-Based Characterization of Train-to-Infrastructure 2.6 GHz Propagation Channel in a Modern Subway Station

TOMÁS DOMÍNGUEZ-BOLAÑO [ID][1]**, JOSÉ RODRÍGUEZ-PIÑEIRO**[2]**,**
JOSÉ A. GARCÍA-NAYA [ID][1]**, (Member, IEEE), XUEFENG YIN** [ID][2]**, (Member, IEEE),**
AND LUIS CASTEDO [ID][1]**, (Senior Member, IEEE)**
[1]Department of Computer Engineering, Faculty of Computer Science, Universidade da Coruña, 15071 ACoruña, Spain
[2]College of Electronics and Information Engineering, Tongji University, Shanghai 201804, China

Corresponding author: José Rodríguez-Piñeiro (j.rpineiro@tongji.edu.cn)

ABSTRACT Channel characterization is essential when planning wireless communication deployments. We consider the wireless channel characterization in a modern subway station and its corresponding entrance tunnel, a topic greatly overlooked in the literature. We setup a Long-Term Evolution (LTE) Evolved NodeB (eNodeB) transmitter in the middle of the platform of a modern station in the Madrid Metro, Spain, to cyclically transmit frequency-division duplex (FDD) LTE signals at a carrier frequency of 2.6 GHz with a bandwidth of 10 MHz. Two receivers were used to investigate both the eNodeB-train and the eNodeB-mobile links. The train was moving at a constant speed of 18 km/h from the entrance tunnel until it is completely stopped at the end of the station. Using the multipath components extracted with the space-alternating generalized expectation-maximization (SAGE) algorithm, we characterized the wireless channel response for both links based on the following parameters: power delay profile, root mean square delay spread, Doppler power spectral density, small-scale fading distribution, and K-factor.

INDEX TERMS Broadband communication, communication, railway communication, communication channels, time-varying channels.

I. INTRODUCTION

With the continuous growth and expansion of cities, subways are gaining importance as they are considered the most efficient transportation system for commuter users [1]–[5]. During transportation, people intensively employ mobile devices to work, to access social networks, or for entertainment purposes. Vehicles also produce mobile data, deserving special consideration safety-related applications since they impose stringent requirements on aspects such as reliability and low latency, although demanding relatively low throughputs [5], [6]. Also, radio communications are required to provide subway users and staff with voice and data-based services.

Leaky feeders are one of the most popular technologies to provide wireless communications in tunnels. Although they do not require sophisticated channel models for system planning, they are unreliable in case of fire, breaking down

communications in the entire tunnel [7]. Moreover, leaky feeders become rather expensive for systems operating at high carrier frequencies, whereas maintenance becomes tedious once tunnels are under operation [8]. Using antennas instead of leaky feeders solves those problems. Antennas offer easier maintenance, a much higher upper frequency limit, a larger distance between repeaters, and they are ten times cheaper to deploy [8]. However, antennas require more sophisticated channel models for system design and planning to assure that quality of service (QOS) requirements are fulfilled.

Many channel models describing radio waves propagation inside tunnels were proposed in the literature (see [7], [9] and the references therein). Most of them consider typical frequencies used for public wireless systems such as GSM, UMTS, Wi-Fi, or LTE. Basically, channel models for tunnels can be classified into two main groups: deterministic
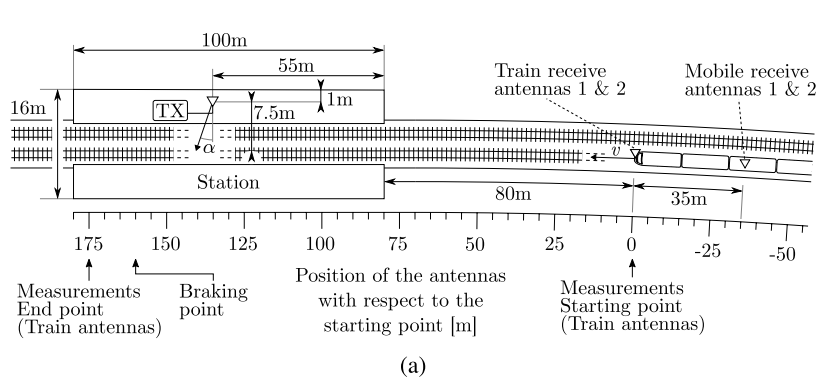
FIGURE 1. (a) Schematic of the measurement scenario (not at scale) at "La Almudena" subway station, Madrid Metro, Spain. The scenario consists of a modern subway station and its corresponding entrance tunnel. (b) Picture taken from the train cabin while conducting measurements. The train is at the measurement starting point with the station visible at the end.

or empirical. Deterministic channel models use mathematical expressions to predict channel characteristics. Usually, three different deterministic approaches are distinguished in the literature: models based on solving Maxwell's equations [10]–[14], models based on modal analysis [15]–[20], and models based on geometric optics (GO) [21]–[25]. On the other hand, empirical models are based on measurements, as the widely used two-slope channel model [17], [26]–[28].

However, characterizing and modeling wireless channels for subway stations and the corresponding entrance tunnel is a topic which has been greatly overlooked in the literature. In this regard, although not oriented to subway stations, the delay spread and path loss for 900 MHz and 2.1 GHz when entering tunnels were studied based on GO in [29]. Also, an analysis of different channel parameters such as power delay profile (PDP), root mean square (RMS) delay spread and path loss based on measurements and GO modeling for a receiver entering a tunnel was carried out in [25]. The path-loss characteristics in subway tunnels at 2.65 GHz were also studied in [30]. More recently, a measurement campaign was carried out in underground subway environments in Shanghai, China, and a channel model was developed for tunnel and station environments based on the clusters of the obtained channel impulse responses [31].

The Madrid Metro in Spain was the scenario of the channel measurements described in [32] and [33]. On the one hand, [32] details the wideband propagation modeling results (mainly mean power and delay spread) obtained from an extensive campaign of static wideband propagation measurements at 980 MHz and 2450 MHz carrier frequencies using a channel sounder. On the other hand, [33] describes the measurements carried out with two different testbeds. One of the testbeds was used to estimate both the signal-to-noise ratio (SNR) and the throughput of Mobile WiMAX transmissions, hence not focusing on channel characterization. The other testbed was used with a twofold objective. Firstly, the path loss was characterized based on narrowband measurements at 980 MHz, 2.4 GHz, and 5.7 GHz carrier frequencies for straight and curved tunnels and inside the station.

Secondly, the PDP was estimated considering wideband signals at 1 GHz and 2.45 GHz carrier frequencies with the channel sounder transmitter and receiver installed on the station platform, not considering the tunnel nor its entrance. Notice that the channel responses in [32] and [33] were obtained using conventional techniques such as the narrow pulse technique, avoiding more powerful approaches such as the SAGE technique proposed in this work and also in [31].

In this work we characterize the wireless channel at 2.6 GHz in "La Almudena" subway station[1] and its entrance tunnel (see Fig. 1). The main contributions and novelties of this paper are detailed below:

1) We consider a LTE eNodeB transmit antenna located at the center of the platform and two receive antenna sets placed, respectively, inside and outside the subway train. We transmit standard-compliant FDD LTE signals at 2.6 GHz with a 10 MHz bandwidth. During the measurements, the train moves from the entrance tunnel to the end of the station at a constant speed of 18 km/h, whereas the transmit signals are recorded continuously at the sampling frequency of $f_s = 15.36$ MHz. In contrast to the measurement-based channel characterizations provided in [34] and [35], the delays, Doppler frequencies, and complex-valued amplitude coefficients of the multipath channel response components are estimated from the standard-compliant FDD LTE signals by means of the SAGE technique as described in [35].

2) The most important channel parameters—such as PDP, RMS delay spread, Doppler power spectral density (PSD), small-scale fading distribution, and K-factor—are estimated from the channel impulse response estimates obtained with the SAGE technique. We considered both outdoor and indoor receive antennas, which enables us to characterize two different links: the eNodeB-train and the eNodeB-mobile links. The eNodeB-train link (direct communication between an

[1]Line 2 of "Metro de Madrid", Madrid subway, Spain.
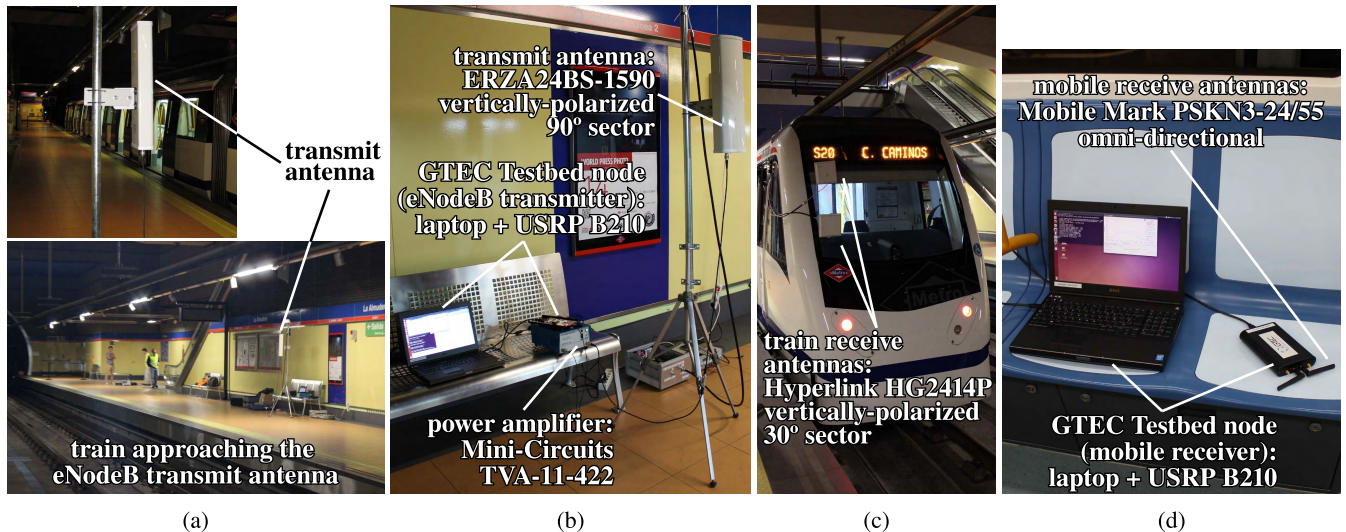
FIGURE 2. GTEC Testbed nodes and antennas used in the measurements: (a) eNodeB transmit antenna on the platform (top) and panoramic view of the platform (bottom). (b) GTEC Testbed node placed on a station bench and configured as an eNodeB transmitter with the corresponding antenna. (c) receive antennas of the eNodeB-train link placed on the train front window. (d) GTEC Testbed node placed on a train bench and configured as the receiver of the eNodeB-mobile link.

eNodeB and the outdoor receive antennas attached to the front window of the train cabin) would be the one used for the transmission of critical data and possibly to support passenger service provisioning based on a relay scheme (see [36]). On the other hand, the eNodeB-mobile link evaluation allows for characterizing the direct communication between a mobile user inside the train carriage and an eNodeB placed on the station platform.

3) We provide the mathematical description of all the procedures followed to obtain the results. In particular, mathematical descriptions are provided to obtain the estimated channel response parameters, such as PDP, RMS delay spread and Doppler PSD, from the delays, Doppler frequencies, and complex-valued amplitude coefficients of the multipath components estimated by the SAGE algorithm.

Although the measurement setup considered in this work is the same as that described in [33], both works are essentially different. Firstly, we consider in this work LTE instead of WiMAX transmissions. Secondly, the WiMAX transmissions in [33] were used to estimate SNR, error vector magnitude (EVM), and throughput, but not to characterize the wireless channel.

The rest of this work is organized as follows. Section II describes the experimental setup. Section III explains the signals used for transmission and the signal processing at the receiver based on the SAGE algorithm. Section IV presents and discusses the wireless channel characterization based on the PDP, the RMS delay spread, the Doppler PSD, the small-scale fading distributions, and the K-factor estimated from the measurements. Finally, Section V is devoted to the conclusions.

II. EXPERIMENTAL SETUP
A. MEASUREMENT ENVIRONMENT
The measurement campaign took place in "La Almudena" subway station and its entrance tunnel (see Fig. 1), which is a representative example of a modern subway station. A schematic and a picture of this measurement scenario are respectively shown in Figs. 1a and 1b, whereas a 3D model of a typical modern subway station of the Madrid Metro can be found in [33, Fig. 2]. "La Almudena" station is 100 m long and the eNodeB transmit antenna (see Figs. 2a and 2b) is located approximately in its center, 55 m away from one of its edges. Although the entrance tunnel is slightly curved, we do not take it into account since such a curvature is small (see Fig. 1b).

For the eNodeB-train link, two antennas were placed outdoors on the train front window (see Figs. 1a and 2c). For the eNodeB-mobile link, two antennas were placed inside the train car, 35 m apart from the eNodeB-train receive antennas (see Figs. 1a and 2d). To reference the position of the antennas along the track we set the arbitrary point 0 to the location of the train antennas (eNodeB-train link) at the measurement starting point (see Fig. 1a), where the train was moving forward at a constant speed of $v = 18$ km/h, and it maintained the speed until it started to brake about 10 m before stopping, and thus ending the measurements. Signals for both the eNodeB-train and the eNodeB-mobile links where captured simultaneously. Therefore, for the train antennas, the measurement started at position 0, whereas for the mobile antennas the measurement started at position -35 m (see Fig. 1a).

The measurement trajectory is further divided into several sections for both the eNodeB-train and the eNodeB-mobile links depending on the train position:

- **eNodeB-train link**: The position of the train outdoor antennas during the measurements ranges from 0 m to 175 m (see Fig. 1a). Note that this position is also the distance traveled by the train during the measurements. We identify the following sections:
  - **Tunnel**: From 0 m to 80 m, the train antennas are inside the station entrance tunnel (see Fig. 1b).
  - **Station (1)**: From 80 m to 135 m, the train antennas are inside the station before passing in front of the eNodeB transmit antenna (see Fig. 2a).
  - **Station (2)**: From 135 m to 160 m, the train antennas are inside the station after passing in front of the transmit antenna and before the train starts braking.
  - **Braking**: From 160 m to 175 m, the train brakes to finally stop.
- **eNodeB-mobile link**: The two antennas (see Fig. 2d) are located inside the train car and placed 35 m apart from the eNodeB-train receive antennas. Hence, the locations of these antennas during the measurements range from −35 m to 140 m (see Fig. 1a). We identify the following sections:
  - **Tunnel:** From −35 m to 80 m, the mobile antennas are inside the entrance tunnel.
  - **Station:** From 80 m to 140 m, the mobile antennas are inside the station. In this case, the train starts braking a little before the mobile antennas reach the position of the transmit antenna. Once the train is stopped, the mobile antennas are located 5 m after passing in front of the transmit antenna.
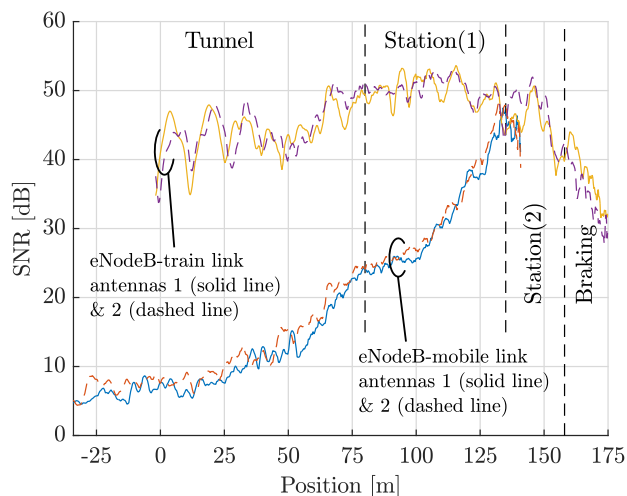
FIGURE 3. SNR for the eNodeB-train and eNodeB-mobile links. Note that the sections specified in the picture refer to the eNodeB-mobile link.

Fig. 3 shows the SNR values along the train trajectory for the eNodeB-train and the eNodeB-mobile links. Such SNR curves were estimated in the time domain and smoothed by a moving average using a window length of 20λ, where λ is the wavelength at the carrier frequency of 2.6 GHz. We can see that, for the mobile antennas, the highest SNR values are obtained when such antennas pass in front of the eNodeB

transmit antenna. However, for the train antennas, due to their high directivity (see Section II-B), the SNR does not vary significantly along the "Station (1)" section.

B. MEASUREMENT EQUIPMENT AND PROCEDURE

For the generation, transmission, acquisition and processing of LTE signals, the so-called GTEC Testbed[2] was used. Notice that the GTEC Testbed has been extensively used in many vehicular measurement campaigns [33], [40]–[46]. More specifically, one node was placed at the subway station to serve as an eNodeB (see Figs. 2a and 2b) which cyclically transmits the same LTE signal specified in Table 1, whereas two nodes were configured as receivers: one is attached to the train antennas placed on the train front window (see Fig. 2c) which corresponds to the eNodeB-train link, whereas the other is connected to the mobile antennas (see Fig. 2d) and corresponds to the eNodeB-mobile link. Although the GTEC Testbed supports time and frequency synchronization among nodes via GPS, this is not possible in underground scenarios, hence the two receivers and the transmitter were not synchronized between them.

TABLE 1. FDD-LTE testbed configuration parameters.

Parameter	Value
Transmit power	18.5 dBm (at input antenna port)
Sampling frequency	15.36 MHz
Carrier frequency	2.6 GHz
Bandwidth	10 MHz (9 MHz occupied)
Number of subcarriers	1024 (600 used)
Cyclic prefix length	Normal [37]*

* For each LTE frame slot (a slot occupies half a subframe), the cyclic prefix length is 80 samples (5.2083 microseconds), whereas for the remaining six orthogonal frequency-division multiplexing (OFDM) symbols it is reduced to 72 samples (4.6875 microseconds).

1) eNodeB TRANSMITTER

The GTEC Testbed node serving as the eNodeB transmitter employs a Mini-Circuits TVA-11-422 power amplifier [47] and a vertically polarized 90° sector antenna "ERZA24BS-1590" (see Figs. 2a, 2b and 4a). Note that the eNodeB antenna was not completely perpendicular to the track, but a small angle of $\alpha \approx 10°$ was considered (see Fig. 2a). The transmit power at the input antenna port was set to 18.5 dBm.

2) eNodeB-TRAIN LINK EQUIPMENT

Two vertically polarized 30° sector "Hyperlink Technologies HG2414P" antennas [48] (see Figs. 2c and 4b) were attached to the train front window. Note that the antenna placement is not optimal in the sense that a deep loss of the received power is expected once the train passes in front of the transmit antenna due to the high directivity of the receive antennas as
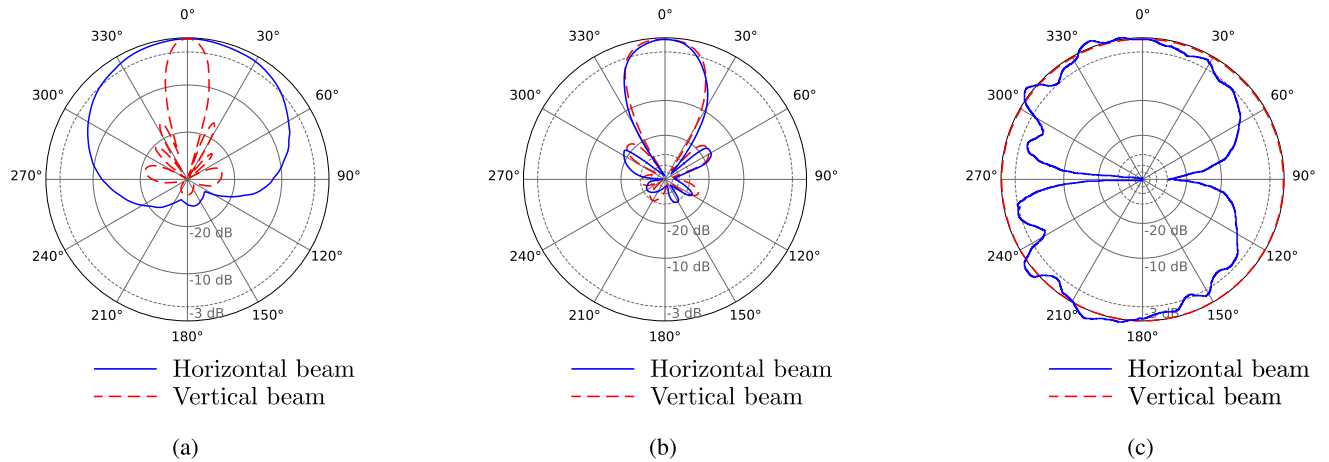
FIGURE 4. Radiation patterns for: (a) eNodeB transmit antenna; (b) train antennas (eNodeB-train link); and (c) mobile antennas (eNodeB-mobile link).

well as the blocking effect of the whole train that obstructs the direct line-of-sight (LoS). Unfortunately, for safety reasons and considering the dimensions of the tunnel, the antennas could not be placed on top of the train or attached to its lateral. Notice also that a similar setup employing the same antennas was considered in [32].

3) eNodeB-MOBILE LINK EQUIPMENT

Two omni-directional and linearly-polarized "Mobile Mark PSKN3-24/55" antennas (see Figs. 2d and 4c) were located inside the train car, 35 m away from the train antennas (see Fig. 1a).

III. RECEIVER SIGNAL PROCESSING

Many of the results presented in this paper depend on the wireless channel response estimates obtained from the received LTE signals. The first step is to detect and synchronize the received LTE frames, which is performed by taking advantage of the Primary Synchronization Signal (P-SCH) and the Secondary Synchronization Signal (S-SCH) (see [37, Sec. 6.11] and [49]). LTE frames are detected and their time offsets are estimated by correlating the received signal with the P-SCH and the S-SCH associated to the configured eNodeB. The time offsets (or synchronization points) for each frame i, namely κ_i, are just the sample number over the discrete-time received signal where the frame was detected. However, in our case, the measurements obtained from the mobile antennas exhibit a very low SNR in the tunnel section, hence the time offsets estimated for those signals could be inaccurate or even totally wrong. Therefore, to obtain a more accurate estimation of the time offsets, and given that LTE signals are acquired continuously, we apply a robust fit linear regression method [50] to the estimated time offsets from the LTE synchronization signals. Finally, the time offsets for each of the LTE frames are obtained from the robust fit regression line.

The channel response for each LTE frame is estimated by means of the SAGE algorithm, which allows for extracting

the parameters of the multipath components of the channel impulse response (see [35] for details of the SAGE algorithm). The model of the channel impulse response for the ith LTE frame is formulated as

$$h_i(t, \tau) = \sum_{l=1}^{M} \alpha_{i,l} \exp\{j2\pi \nu_{i,l} t\} \delta(\tau - \tau_{i,l}), \qquad (1)$$

where t is the time variable, τ is the delay variable, M is the number of waves or paths considered, and $\delta(\cdot)$ is the Dirac delta function. The parameters estimated by the SAGE algorithm are $\alpha_{i,l}$, $\nu_{i,l}$, and $\tau_{i,l}$, being $\alpha_{i,l} \in \mathbb{C}$ the lth-path amplitude, and $\nu_{i,l} \in \mathbb{R}$ and $\tau_{i,l} \in \mathbb{R}$ the respective Doppler frequency and delay for the lth path.

To estimate the channel with the SAGE algorithm, the time offsets are used to pick each of the individual frames and pass them to the algorithm. Therefore, the domain of t in (1) is $[0, T)$, being $T = 10$ ms the duration of an LTE frame, and the obtained delays $\tau_{i,l}$ are relative delays. To obtain the absolute delays we take into account the time offsets κ_i and the scenario geometry. However, as said before, note that the GTEC Testbed nodes were not synchronized in time nor in frequency due to the lack of GPS coverage inside the station. This introduces an additional error in the obtained time offsets with respect to the expected ones. Therefore, the absolute time delay for the lth tap of the ith frame, namely $\tilde{\tau}_{i,l}$, is obtained as

$$\tilde{\tau}_{i,l} = \tau_{i,l} + (\kappa_i - i \cdot N_s - \kappa_0)/f_s + i \cdot m + b, \qquad (2)$$

where N_s is the number of samples of an LTE frame, b is the absolute delay of the first received LTE frame, and m is a factor (expressed in seconds per frame) to correct the error of the obtained delay. Based on the scenario geometry, considering that the path followed by the train is an straight line, the expected delay of the signals for a given time t is

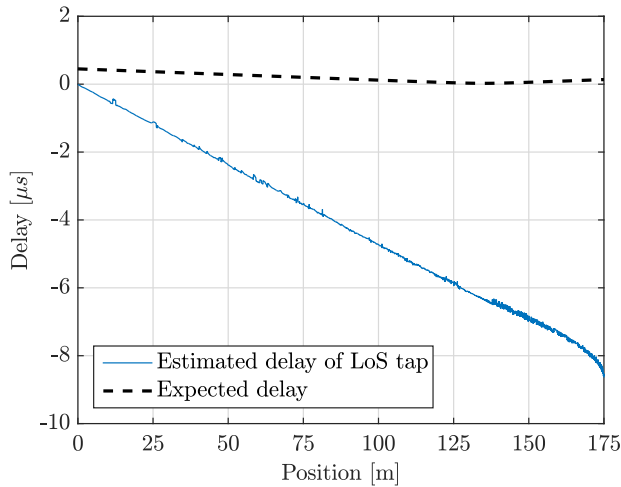$$\tau_{\exp}(t) = \frac{\sqrt{(x_a - vt)^2 + x_p}}{c}, \qquad (3)$$

FIGURE 5. Estimated delay of the LoS path for the eNodeB-train link, antenna 1, before correction as indicated in (2).
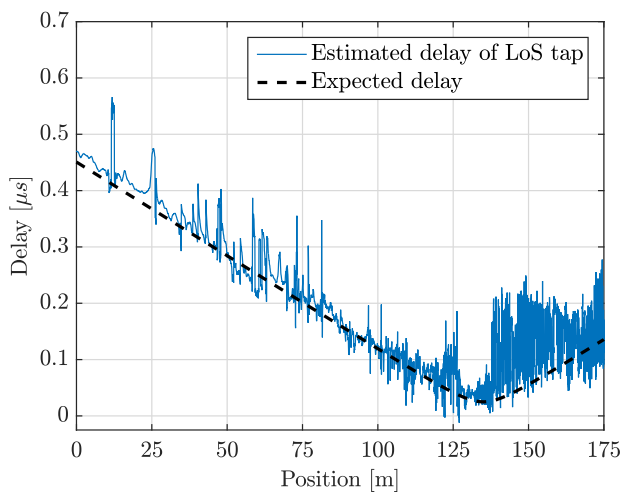

FIGURE 6. Estimated delay of the LoS path for the eNodeB-train link, antenna 1, after correction as indicated in (2).

where v is the speed of the train (given that in our measurements $v = 18$ km/h is constant, then vt is the distance traveled), $x_a = 135$ m is the position of the transmitter, $x_p = 7.5$ m is the perpendicular distance between the transmitter and the track (see Fig. 1a), and c is the speed of light. In Fig. 5 we show the delay of the LoS tap for the antenna 1 of the eNodeB-train link before correction (hence, $m = 0$ and $b = 0$ in (2)), as well as the expected delay defined in (3). Based on the expected delay, we select the values of m and b in (2) to obtain the correct absolute delay values. Fig. 6 shows the delay of the LoS tap once the correction is applied together with the expected delay, revealing that now the estimated delay matches the expected one. Therefore, we define the corrected channel impulse response as

$$\tilde{h}_i(t, \tau) = \sum_{l=1}^{M} \tilde{\alpha}_{i,l} \exp\{j2\pi \tilde{v}_{i,l} t\} \delta(\tau - \tilde{\tau}_{i,l}), \quad (4)$$

where $\tilde{\tau}_{i,l}$ is the corrected delay defined in (2), $\tilde{\alpha}_{i,l} = \alpha_{i,l}$ and $\tilde{v}_{i,l} = v_{i,l}$.

Regarding the channel parameter estimation, as detailed in [35], we consider a sequence of N equally spaced orthogonal frequency-division multiplexing (OFDM) symbols for each LTE frame. For the eNodeB-train link received signals we use $N = 5$ OFDM symbols, whereas for the eNodeB-mobile link signals we consider different values of N ranging from $N = 5$ for the frames with the highest SNR to $N = 140$ for the frames with lowest SNR (e.g, inside the tunnel). For both links, we estimated $M = 15$ paths using 10 iterations of the SAGE algorithm. Considering that an LTE frame lasts for 10 ms, for the worst case considered with $N = 5$ the Doppler frequency estimation range is $[-200, 200]$ Hz. In our scenario, the train velocity is 18 km/h and hence the theoretically maximum absolute Doppler shift is 43.33 Hz at a carrier frequency of 2.6 GHz, which is within the estimation range. Also, during the 10 ms LTE frame duration the train travels 0.05 m, which is much less than the distances between the transmitter antenna, scatters, and the receive antenna. Therefore, we assume that the channel remains stationary during the duration of a single LTE frame, thus enabling the estimation of the dominant paths parameters using the SAGE algorithm [51].

Considering again that the LTE frame duration is 10 ms, we define the channel impulse response for the whole train trajectory, which is obtained by concatenating the different $\tilde{h}_i(t, \tau)$, as follows:

$$h(t, \tau) = \tilde{h}_{\lfloor t/(10 \text{ ms})\rfloor}(t - \lfloor t/(10 \text{ ms})\rfloor \cdot 10 \text{ ms}, \tau), \quad (5)$$

where $\lfloor \cdot \rfloor$ is the floor operator.

IV. MEASUREMENT RESULTS

In this section we show the results obtained from our measurements, both for the eNodeB-train and the eNodeB-mobile links. These results are the path loss, the power delay profile (PDP), the root mean square (RMS) delay spread, the Doppler power spectral density (PSD), the small-scale fading distribution, and the K-factor. Such results constitute an empirical characterization of the channel experienced by both links as the train approaches and enters the station. Note that for obtaining these results the impact of the antenna patterns has not been removed from the measurement data.

A. PATH LOSS ESTIMATION
The path loss is the ratio between the transmitted and the received power values expressed in decibels [52]

$$\text{PL}(d) = 10 \log_{10}\left(\frac{P_t}{P_r(d)}\right), \quad (6)$$

where $\text{PL}(d)$ is the path loss for a distance d, P_t is the transmit power, and $P_r(d)$ is the received power at a distance d. The path loss can be modeled by a simple log-distance model [52], which we will use here and is expressed in decibels as

$$\begin{aligned}
\text{PL}(d) &= \overline{\text{PL}}(d_0) + 10\gamma \log_{10}\left(\frac{d}{d_0}\right) + X_\sigma \\
&= b + 10\gamma \log_{10} d + X_\sigma, \quad (7)
\end{aligned}$$

TABLE 2. Path loss estimated parameters for the double breakpoint model (estimating d_1).

Antenna	γ_1	γ_2	b_1	b_2	d_1	σ_1^2	σ_2^2	MSE
mobile 1	2.590	3.694	38.819	20.337	47.181	2.800	1.184	2.412
mobile 2	2.614	3.702	37.564	18.930	51.531	3.011	0.595	2.370
train 1	-0.709	1.773	79.905	41.816	34.270	7.048	2.395	6.053
train 2	-0.329	2.037	74.801	36.433	41.865	6.632	2.334	5.462

where d_0 is the so-called "break distance" (a reference distance relatively close to the transmitter [52]), $\overline{PL}(d_0)$ is the mean path loss at the distance d_0, γ is the path loss exponent, and X_σ is a zero-mean Gaussian random variable. For simplicity, we factorize the d_0 terms into the intercept term $b = \overline{PL}(d_0) - 10\gamma \log_{10}(d_0)$. Note that antenna gains are included in the path loss results.

Moreover, in our scenario, the transition from the tunnel to the station changes the signal propagation characteristics. Therefore, a two-breakpoint path loss model [52] is more suitable and is defined as

$$PL(d) = \begin{cases} b_1 + 10\gamma_1 \log_{10}(d) + X_{\sigma,1}, & \text{if } d_0 \leq d \leq d_1 \\ b_2 + 10\gamma_2 \log_{10}(d) + X_{\sigma,2}, & \text{if } d_1 \leq d, \end{cases}$$
(8)

where we have two different regions with intercepts b_1 and b_2, path loss exponents γ_1 and γ_2, and zero-mean Gaussian random variables $X_{\sigma,1}$ and $X_{\sigma,2}$. Note that a consequence of this model is that the following equality must hold

$$\overline{PL}(d_1) = b_1 + 10\gamma_1 \log_{10}(d_1) = b_2 + 10\gamma_2 \log_{10}(d_1). \quad (9)$$

Therefore, we considered the following path loss models:

1) Single breakpoint model defined in (7). The intercept b and the path loss exponent γ are estimated by means of a least-squares fitting.
2) Double breakpoint model defined in (8). The intercept b_1, the path loss exponents γ_1 and γ_2, and the distance d_1 are estimated by a least-squares fitting. The intercept b_2 is obtained by means of (9).

TABLE 3. Path loss estimated parameters for the single breakpoint model.

Antenna	γ	b	σ^2	MSE
mobile 1	3.230	29.795	3.269	3.269
mobile 2	3.198	29.242	3.226	3.226
train 1	0.924	58.180	9.360	9.360
train 2	0.982	56.885	8.874	8.874

The results obtained from the single and double breakpoint models are shown in Tables 2 and 3, respectively. According to the mean square error (MSE), the double-breakpoint model provides a much better fit than the single-breakpoint one. For the eNodeB-mobile link, the results from the double-breakpoint model are very similar for both antennas (see Table 2), the MSE values are almost equal, and the estimated values for d_1 (47.181 m and 51.531 m) are relatively close to

the actual distance to the tunnel (55.51 m). For the eNodeB-train link (outdoor receive antennas), the estimated d_1 values for antennas 1 and 2 are 34.270 m and 41.865 m, respectively. In this case, the estimated distances are not so close to the actual ones because of the high directivity of the receive antennas, which makes the receive power to depend not only on the distance but also on the respective angles between the receive and transmit antennas.
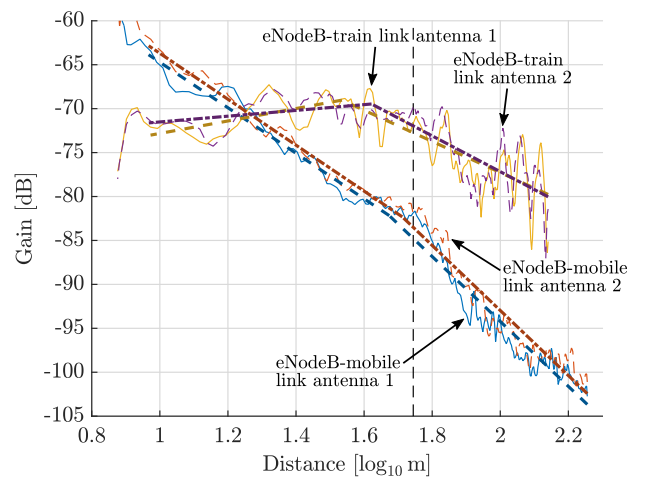
FIGURE 7. Gain ($-PL(d)$) for the eNodeB-train and eNodeB-mobile links. Fittings obtained with the two-breakpoint model are shown in black dashed lines for antennas 1 and dot-dashed lines for antennas 2.

Fig. 7 shows the estimated gain (negative path loss) for all the four receive antennas considered. We plot superimposed the fittings of the double-breakpoint model (estimating also d_1). The curves shown in the Fig. 7 were smoothed using a moving average with a window length of 20λ (at the carrier frequency of 2.6 GHz). A clear change in the propagation characteristics for tunnel and station scenarios can be appreciated for both the eNodeB-train and the eNodeB-mobile links. Tables 2 and 3 show that path loss exponents for the train antennas are slightly greater than 2 (free space). The results are coherent with those shown in [30], although the path loss exponent in [30] is slightly lower than 2. Note that the estimated path loss exponents for the station section (γ_1) become negative due to the high directivity of the receive antennas, which causes the received power to become larger for longer distances if the beams of the transmit and receive antennas are better aligned than for shorter distances. Path loss exponents for the eNodeB-mobile link for the train station are lower than those measured in [41], which found that $\gamma = 3.81$ at 2.4 GHz in a completely non-enclosed train station.
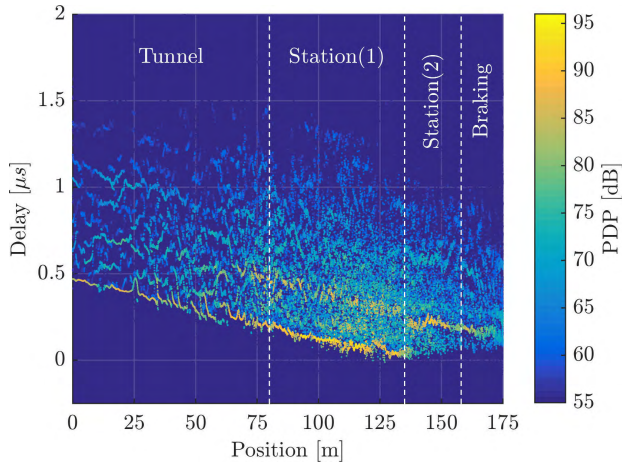
FIGURE 8. PDP scatter plot for the eNodeB-train link along the train trajectory (antenna 1).
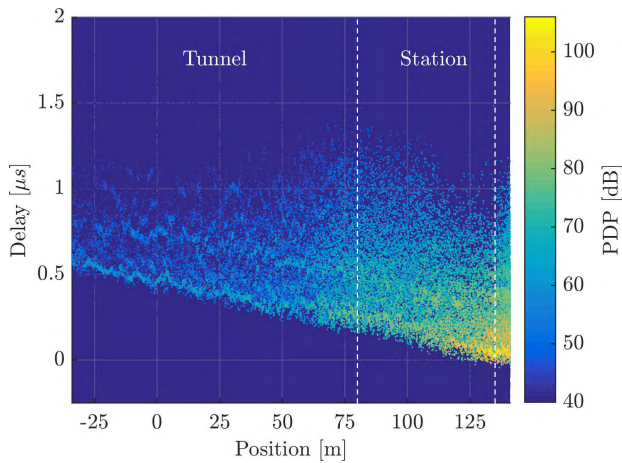

FIGURE 9. PDP scatter plot for the eNodeB-mobile link along the train trajectory (antenna 1).

B. POWER DELAY PROFILE

The PDP contains information about how much power arrives at the receiver with a certain delay τ. In practice, the PDP is obtained as the power for a certain timespan over which the channel is quasi-stationary [53]. In our case, we calculate the PDP for each acquired LTE frame from the channel estimates produced by the SAGE algorithm (see (4)), thus obtaining the "instantaneous" PDP. Following [54], we define the "instantaneous" PDP for the ith LTE frame as

$$P_i(\tau) = \sum_{l=1}^{M} |\tilde{\alpha}_{i,l}|^2 \, \delta\left(\tau - \tilde{\tau}_{i,l}\right). \tag{10}$$

Figs. 8 and 9 show, respectively, the PDP for the eNodeB-train and the eNodeB-mobile links. The PDPs are drawn using a scatter plot where each point corresponds to the power of a single path, as shown in (10). The slope exhibited by the PDP curves accounts for the propagation delay.

We also calculate the so-called normalized mean PDP for the considered sections as the mean PDP after removing the propagation delay. The normalized mean PDP is useful in link-level and system-level simulations where the path

loss is modeled from the scenario geometry and the small-scale fading characteristics are extracted directly from the measurements.

The estimated propagation delay is computed by applying a robust fit algorithm with the delay of the most powerful taps of the LTE frames for each section, yielding the slope $\tilde{m}$ and intercept $\tilde{b}$. Next, to obtain the normalized mean PDP for each section, we sample the time-varying channel impulse response in the delay domain, hence obtaining the equivalent continuous-time versus discrete-delay channel impulse response. We just use a simple interpolation with a rectangular low-pass filter (convolution with a sinc pulse in the delay domain). Hence, the channel impulse response for the ith LTE frame is expressed as

$$
\begin{aligned}
\hat{h}_i&(t, n_\tau) \\
&= \frac{1}{\sqrt{f_\tau}} \left(\tilde{h}_i(t, \tau) * \text{sinc}((\tau - \tilde{m}i - \tilde{b})f_\tau) \right)(n_\tau/f_\tau) \\
&= \frac{1}{\sqrt{f_\tau}} \int_{-\infty}^{\infty} \tilde{h}_i(t, u) \cdot \text{sinc}((n_\tau/f_\tau - u - \tilde{m}i - \tilde{b})f_\tau) \text{d}u \\
&= \frac{1}{\sqrt{f_\tau}} \sum_{l=1}^{M} \tilde{\alpha}_{i,l} \exp\{j2\pi \tilde{v}_{i,l}t\} \\
&\quad \cdot \text{sinc}(n_\tau - (\tilde{\tau}_{i,l} + \tilde{m}i + \tilde{b})f_\tau),
\end{aligned} \tag{11}
$$

where f_τ is the sampling frequency, $n_\tau = \tau/f_\tau$ such that $n_\tau \in \mathbb{Z}$ is the corresponding discrete-time index for the delay τ, $*$ is the convolution operator, and sinc is the normalized sinc function defined as $\text{sinc}(t) = \sin(\pi t)/\pi t$. Note that, since the channel impulse response in (4) is expressed as a sum of delta functions, it is not band-limited. Since the impulse responses are estimated from the LTE received signal with a 10 MHz bandwidth, f_τ should be higher than 10 MHz. However, considering values much higher than f_τ will not provide additional relevant information. For the results presented below we used $f_\tau = 10 f_S$, where $f_S = 15.36$ MHz is the LTE signal sampling frequency. Then, the normalized mean sampled PDP for the ith LTE frame is

$$P_i[n_\tau] = \frac{1}{T} \int_0^T \left| \hat{h}_i(t, n_\tau) \right|^2 \text{d}t, \tag{12}$$

where $T = 10$ ms is the duration of an LTE frame. Assuming that the channel is stationary, the formula is generalized to

$$
\begin{aligned}
P_i[n_\tau] &= \lim_{T \to \infty} \frac{1}{2T} \int_{-T}^{T} \left| \hat{h}_i(t, n_\tau) \right|^2 \text{d}t \\
&= \frac{1}{f_\tau} \sum_{l=1}^{M} \left| \tilde{\alpha}_{i,l} \cdot \text{sinc}(n_\tau - (\tilde{\tau}_{i,l} + \tilde{m}i + \tilde{b})f_\tau) \right|^2.
\end{aligned} \tag{13}
$$

Finally, the normalized mean sampled PDP for each section $\mathcal{C}_j$ is obtained by dividing with respect to the total received power:

$$
\begin{aligned}
P_{\mathcal{C}_j}[n_\tau] &= \frac{1}{|\mathcal{C}_j|} \sum_{i \in \mathcal{C}_j} \frac{P_i[n_\tau]}{\sum_{n_\tau=-\infty}^{\infty} P_i[n_\tau]} \\
&= \frac{1}{|\mathcal{C}_j|} \sum_{i \in \mathcal{C}_j} \frac{P_i[n_\tau]}{\sum_{l=1}^{M} |\tilde{\alpha}_{i,l}|^2},
\end{aligned} \tag{14}
$$

where $\mathcal{C}_j$ is the set containing the indices i of the LTE frames received along the jth section. Note that parameters m and b in (11) are calculated for each section $\mathcal{C}_j$ considering the LTE frames with indices $i \in \mathcal{C}_j$.
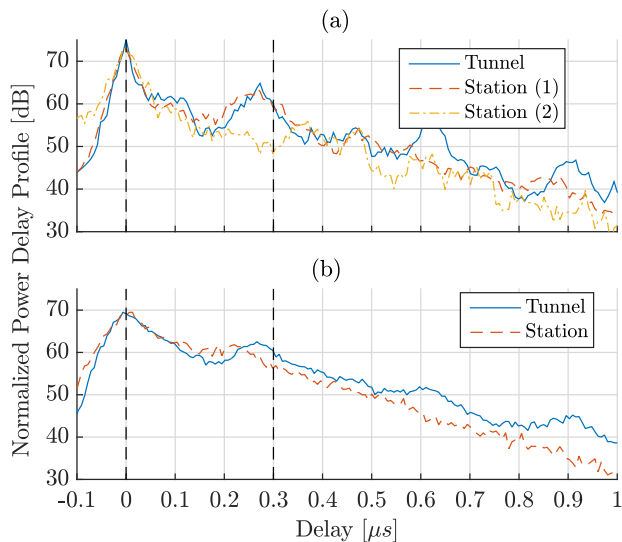

FIGURE 10. Normalized mean PDP (antenna 1).

Figs. 10a and 10b show the normalized mean PDP for the different sections considered for the eNodeB-train and eNodeB-mobile links, respectively. For the eNodeB-train link we see that the PDPs of the "tunnel" and "station (1)" sections are quite similar, and we observe delay clusters that are also coherent with the station geometry (see Fig. 1) and with the results reported in [31, Figs. 4 to 6]. A similar trend is also observed in [33] and [53], although these results were obtained without using the SAGE algorithm. Notice that the most powerful paths correspond to delay $\tau = 0$, marked in Fig. 10 with the leftmost black dashed line. We can also see another peak for these two regions a little bit earlier than $\tau = 0.3\,\mu$s. This delay corresponds to the signal bouncing on the other side of the station and coming back. Considering again the station geometry, the delay of this bounce is, as the best approximation, the time required by the signal to reach the back of the station and come back, which is $2 \cdot 45/c_0 = 0.3\,\mu$s, where c_0 is the speed of light in free space in m/s and 45 m is the distance between the antenna and the back of the station (see Fig. 1a). This delay is also marked in Fig. 10a with the rightmost black dashed line. The main and reflected paths appear clearly in Fig. 8. The "station (2)" section shown in Fig. 10a comes after the train passes in front of the transmit antenna. Fig. 8 shows that the main paths (the paths with lower delay) disappear when the train passes in front of the eNodeB transmit antenna and, after that point, the contribution to the received signal comes exclusively from the paths reflected on the back of the station. As commented above, this effect is due to the high directivity (30°) of the train antennas.

The normalized mean PDPs shown in Fig. 10b for the tunnel and station sections correspond to the eNodeB-mobile
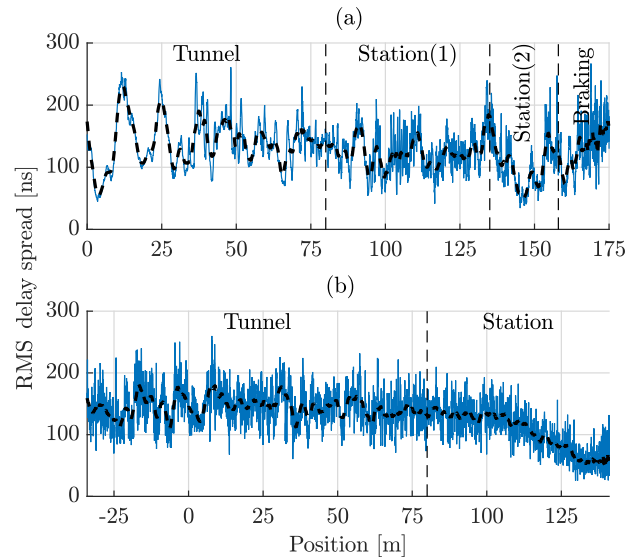

FIGURE 11. RMS delay spread (antenna 1).

link and they are coherent with the scenario geometry, given that the receive antennas are inside the train carriage and that its doors are closed all the time. Only when the mobile antennas are in front of the eNodeB transmit antenna the signal level is sufficiently high to observe significant peaks in the PDP. Again, as in Fig. 10a, the most powerful path is the one at delay $\tau = 0$ (marked in Fig. 10b with the leftmost black dashed line). As for the eNodeB-train link PDP shown in Fig. 10a, the rightmost black dashed curve in Fig. 10b, drawn a little bit before $\tau = 0.3\,\mu$s, corresponds to the delay needed by the signal bouncing on the other side of the station and coming back.

C. ROOT MEAN SQUARE DELAY SPREAD

Another useful parameter to characterize a wireless channel is the RMS delay spread since, under some circumstances, it is proportional to the error probability due to delay dispersion [53]. The RMS delay spread is calculated as the normalized second-order central moment of the delay [53]. Firstly, let us define the normalized PDP for the ith LTE frame as

$$\tilde{P}_i(\tau) = \frac{P_i(\tau)}{\int_{-\infty}^{\infty} P_i(\tau)\mathrm{d}\tau} = \frac{\sum_{l=1}^{M} |\tilde{\alpha}_{i,l}|^2 \delta\left(\tau - \tilde{\tau}_{i,l}\right)}{\sum_{l=1}^{M} |\tilde{\alpha}_{i,l}|^2}. \quad (15)$$
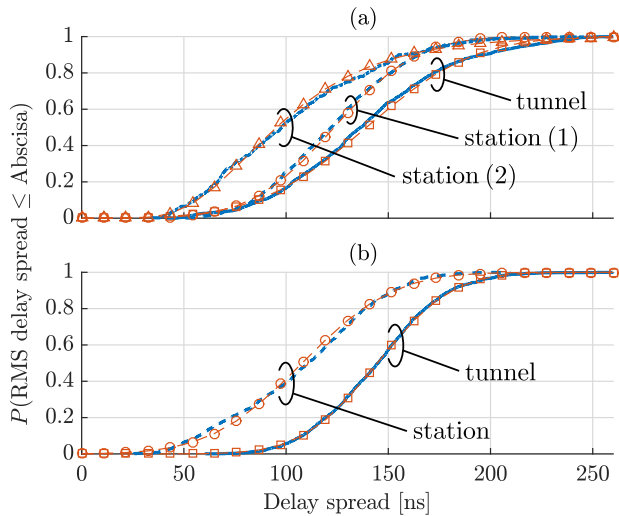
From the result in (15), the nth moment of the delay is

$$\mathbb{E}_i[\tau^n] = \int_{-\infty}^{\infty} \tilde{P}_i(\tau)\tau^n\mathrm{d}\tau = \frac{\sum_{l=1}^{M} |\tilde{\alpha}_{i,l}|^2 \tilde{\tau}_{i,l}^n}{\sum_{l=1}^{M} |\tilde{\alpha}_{i,l}|^2}, \quad (16)$$

and the RMS delay spread is defined as

$$S_i = \sqrt{\mathbb{E}_i[\tau^2] - \mathbb{E}_i[\tau]^2}. \quad (17)$$

Figs. 11a and 11b show the RMS delay spread per frame for both the eNodeB-train and eNodeB-mobile links, respectively. Figs. 11a and 11b also show the smoothed results

FIGURE 12. CDF of the delay spread (antenna 1) and fittings. Empirical CDFs are shown in thick blue lines, fittings of the CDFs are shown in thin red lines with markers. Results for the "braking" section are similar to those of the "tunnel" section and we omit them.

(dashed lines) using a moving average with a window length of 20 λ.

Figs. 12a and 12b show the RMS delay spread cumulative distribution functions (CDFs) for both the eNodeB-train and eNodeB-mobile links, respectively. Different CDFs were calculated for each section. In all cases, the data were fit to a distribution, which are also shown in Figs. 12a and 12b. For the case of the eNodeB-train link we found that, for the "tunnel", "station (1)", and "braking" sections, a normal distribution provides a good fit to the data. However, for the case of the "station (2)" section, a lognormal distribution offers a better fit. On the other hand, for the eNodeB-mobile link, the "tunnel" and the "station" sections are fitted with a normal distribution. Finally, Tables 4 and 5 summarize the fitting results for all antennas and sections of both links.

TABLE 4. RMS delay spread distribution fittings and 90 % value of CDF for the eNodeB-train link. Values are expressed in nanoseconds.

Section	Antenna	90 % value of CDF	Distribution fittings		
			Distribution	μ	σ
Tunnel	1	196.12	Normal	139.29	41.56
	2	195.86		145.74	37.13
Station (1)	1	165.40	Normal	123.53	31.91
	2	160.27		130.35	23.41
Station (2)	1	154.86	Lognormal	4.56	0.40
	2	120.08		4.26	0.41
Braking	1	186.54	Normal	138.97	39.25
	2	216.65		160.49	46.89

Some interesting points about the obtained delay spread results deserve to be emphasized. For the eNodeB-train link, the largest delay-spread variations occur inside the tunnel, where an oscillating pattern is observed. As shown in Fig. 11, this is due to oscillations in the power of the dominant path,

TABLE 5. RMS delay spread distribution fittings and 90 % value of CDF for the eNodeB-mobile link. Values are expressed in nanoseconds.

Section	Antenna	90 % value of CDF	Distribution fittings		
			Distribution	μ	σ
Tunnel	1	180.27	Normal	144.59	28.59
	2	183.85		144.78	31.02
Station	1	152.53	Normal	107.83	35.31
	2	150.79		106.94	36.30

which could be explained by a 2-ray channel model. Exactly at the point where the transmit antenna is placed (marked with a dashed line between "station (1)" and "station (2)" in Fig. 11), the delay spread exhibits a large peak because the LoS signal component is lost at that point (see the PDP around the position marked with the dashed line between the "station (1)" and the "station (2)" sections in Fig. 8). Notice that, analogously to the results reported in [41], the average RMS delay spread does not change significantly from the tunnel to the station. For the case of the eNodeB-mobile link, we can see in Fig. 11b that the mean delay spread decreases noticeably when the mobile receive antennas are in the station.

D. DOPPLER POWER SPECTRAL DENSITY

Analogously to the PDP case, the Doppler PSD function contains information about the power of the signals impinging the receiver with a given Doppler frequency. More specifically, the Doppler PSD is related to the angle of arrivals (AoAs) of the multipath components.

As we did for the PDP, we calculate the Doppler PSD for each received LTE frame from the channel estimates defined in (4) and determined with the SAGE algorithm, thus obtaining the "instantaneous" Doppler PSD. Following an equivalent approach to the one shown in [54] for the PDP, we define the "instantaneous" Doppler PSD for the *i*th LTE frame as:

$$D_i(\nu) = \sum_{l=1}^{M} \left| \tilde{\alpha}_{i,l} \right|^2 \delta \left(\nu - \tilde{\nu}_{i,l} \right). \qquad (18)$$

For each frame *i*, analogously to the mean delay obtained in (16) for $n = 2$, we can also obtain the mean Doppler PSD as:

$$\mathbb{E}_i[\nu] = \frac{\int_{-\infty}^{\infty} D_i(\nu)\nu d\nu}{\int_{-\infty}^{\infty} D_i(\nu)d\nu} = \frac{\sum_{l=1}^{M} \left| \tilde{\alpha}_{i,l} \right|^2 \tilde{\nu}_{i,l}}{\sum_{l=1}^{M} \left| \tilde{\alpha}_{i,l} \right|^2}. \qquad (19)$$

Figs. 13 and 14 show the Doppler PSD for the eNodeB-train and eNodeB-mobile links, respectively. The Doppler PSDs are plotted using an scatter plot where each point corresponds to the power of a single path, as shown in (10). The smoothed mean of the Doppler PSD is also calculated for each frame as in (19) and plotted with a superimposed dashed line. As commented in Section III, the theoretical maximum Doppler shift in our case, at a carrier frequency of 2.6 GHz and a train speed of 18 km/h, is $f_m = 43.33$ Hz.
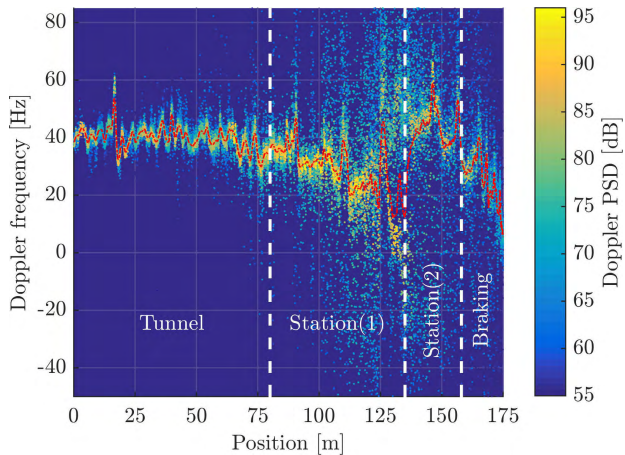
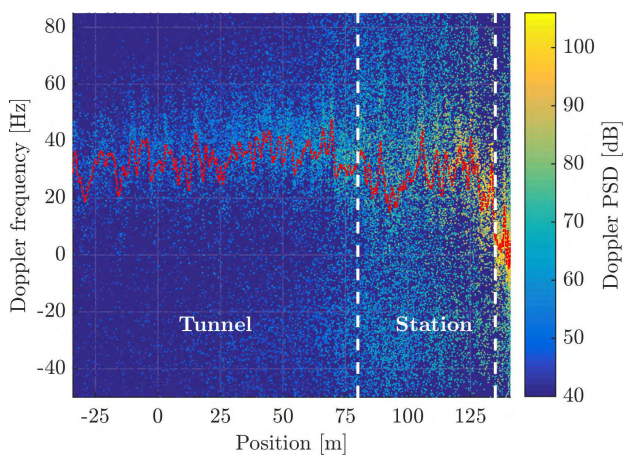**FIGURE 13.** Doppler PSD for the eNodeB-train link (antenna 1).

FIGURE 14. Doppler PSD for the eNodeB-mobile link (antenna 1).

Fig. 13 shows that the mean Doppler PSD for the "tunnel" section exhibits an oscillating pattern, reaching values close to the theoretical maximum Doppler shift f_m. At some points, we can see that the Doppler shift is larger than f_m, an effect explained by multiple bouncing of the incoming signal. In the "station (1)" section we observe how the mean Doppler shift decreases as the train passes in front of the transmitter, as expected. Finally, during the "braking" section, the mean Doppler frequency diminishes due to the speed reduction of the train. For the eNodeB-train link, the Doppler components with a negative frequency are almost nonexistent, even when the train passes in front of the transmitter, due to the high directivity of the train receive antennas.

For the eNodeB-mobile link results shown in Fig. 14, we can see that the Doppler PSD has a much larger variance because the direct LoS component is not present. It is worth noting that, for both the eNodeB-train and the eNodeB-mobile links, the Doppler components are concentrated around the positive frequencies, whereas some components in the negative frequencies arise when the train is in the "station" section.

E. MEAN-CENTERED DOPPLER POWER SPECTRAL DENSITY

One of the first steps in a digital receiver processing chain is to synchronize the received signals, hence estimating and correcting time and frequency offsets between the transmitter and the receiver. In the case of a frequency offset, a frequency shift is typically applied. The estimated frequency offset is the offset due to transmitter and receiver oscillator misalignments plus the mean Doppler frequency of the receive signal. Therefore, to characterize the Doppler PSD that actually impacts on the receiver after the (ideal) frequency offset correction, we subtract the mean Doppler frequency per frame from the calculated Doppler PSD, leading to the mean-centered Doppler PSD, defined as

$$D_i^{MC}(\nu) = D_i(\nu) - \mathbb{E}_i[\nu]. \tag{20}$$

Figs. 15 and 16 show the mean-centered Doppler PSD for both the eNodeB-train and the eNodeB-mobile links, respectively. Fig. 15 shows that the mean-centered Doppler PSD is close to zero almost all the time except for the "station (1)" section once the train passes the 120 m point. Again, this effect is due to the high directivity of the train receive antennas. The mean-centered Doppler PSD shown in Fig. 16 corresponds to the eNodeB-mobile link and is much wider than that observed for the eNodeB-train link (see Fig. 15) since the receive antennas are omni-directional in this case, resulting in a much higher number of acquired multipath components.
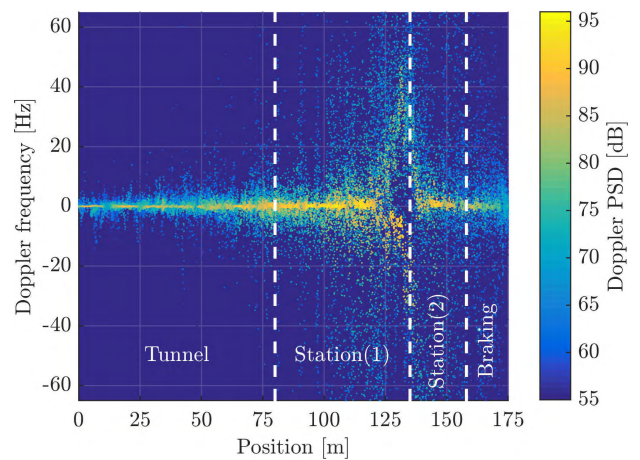

FIGURE 15. Mean-centered Doppler PSD for the eNodeB-train link (antenna 1).

Analogously to the PDP case, we obtain the normalized mean-centered Doppler PSD for the different sections of both scenario links. Firstly, we consider the channel time-frequency response

$$H_i(t, f) = \mathcal{F}_\tau \left(\tilde{h}_i(t, \tau) \right),$$

$$= \sum_{l=1}^{M} \tilde{\alpha}_{i,l} \exp\{j2\pi(\tilde{\nu}_{i,l}t - f\tilde{\tau}_{i,l})\}, \tag{21}$$
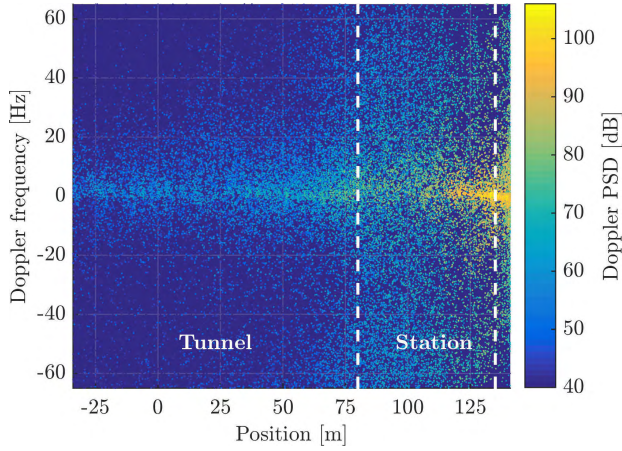
FIGURE 16. Mean-centered Doppler PSD for the eNodeB-mobile link (antenna 1).

with $\mathcal{F}_\tau(\cdot)$ being the Fourier transform with respect to the delay τ. From the time-frequency response we obtain the Doppler-variant transfer function as

$$B_i(v,f) = \mathcal{F}_t(H_i(t,f))$$
$$= \sum_{l=1}^{M} \tilde{\alpha}_{i,l} \delta(v - \tilde{v}_{i,l}) \exp\{-j2\pi f \tilde{\tau}_{i,l}\}. \quad (22)$$

We next proceed as with the PDP to obtain a sampled version of this function by applying an interpolation filter, thus obtaining the sampled Doppler-variant transfer function

$$\hat{B}_i(n_v, f)$$
$$= \frac{1}{\sqrt{f_v}} (B_i(v,f) * \text{sinc}((v f_v)))(n_v/f_v)$$
$$= \frac{1}{\sqrt{f_v}} \int_{-\infty}^{\infty} B_i(v,f)\text{sinc}(n_v)du$$
$$= \frac{1}{\sqrt{f_v}} \sum_{l=1}^{M} \tilde{\alpha}_{i,l} \exp\{j2\pi \tilde{\tau}_{i,l}t\}\text{sinc}(n_v - \tilde{v}_{i,l}f_v). \quad (23)$$

Finally, the mean-centered Doppler PSD is obtained as

$$D_i[n_v] = \lim_{F \to \infty} \frac{1}{2F} \int_{-F}^{F} |\hat{B}_i(n_v - \mathbb{E}_i[v], f)|^2 df$$
$$= \sum_{l=1}^{M} |\tilde{\alpha}_{i,l}\text{sinc}(n_v - \mathbb{E}_i[v] - \tilde{v}_{i,l}f_v)|^2, \quad (24)$$

where f_v is the sampling frequency and $n_v = v/f_v$ is the corresponding discrete-time index for the Doppler frequency v. We finally obtain the normalized sampled Doppler PSD for each section $\mathcal{C}_j$ as

$$D_{\mathcal{C}_j}[n_v] = \frac{1}{|\mathcal{C}_j|} \sum_{i \in \mathcal{C}_j} \frac{D_i[n_\tau]}{\sum_{n_\tau=-\infty}^{n_\tau=\infty} D_i[n_\tau]}$$
$$= \frac{1}{|\mathcal{C}_j|} \sum_{i \in \mathcal{C}_j} \frac{D_i[n_\tau]}{\sum_{l=1}^{M} |\tilde{\alpha}_{i,l}|^2}, \quad (25)$$

where $\mathcal{S}$ is the set containing the indices i of the LTE frames received in the corresponding section. We used $f_v = 2/3$ to calculate the results presented in this section.
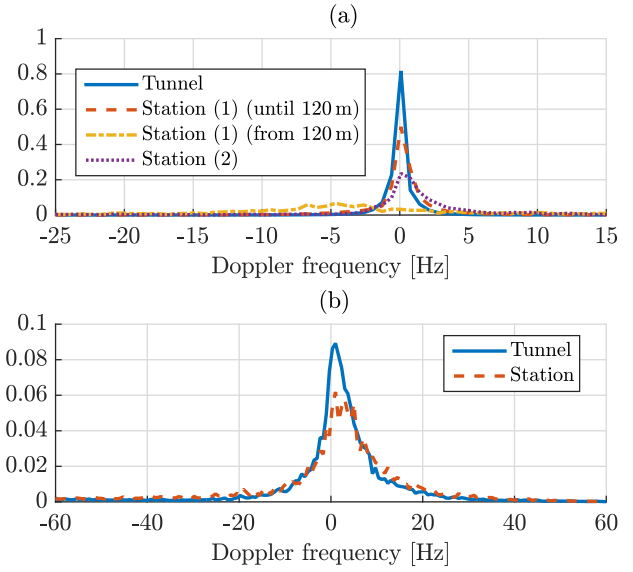

FIGURE 17. Normalized mean-centered Doppler PSD (antenna 1).

Figs. 17a and 17b show the normalized mean-centered Doppler PSD for both the eNodeB-train and the eNodeB-mobile links, respectively. For the case of the eNodeB-train link (Fig. 17a) we divide the results for the "station (1)" in two parts: until 120 m and after 120 m (see Fig.). We observe that the Doppler PSD which effectively degrades the signal after the frequency offset correction (assuming a perfect frequency offset estimation and correction) is larger for the eNodeB-mobile link (see Fig. 17b) than for the eNodeB-train link (see Fig. 17a). In both cases, however, small Doppler shift values are observed, which is consistent with the low speed (18 km/h) of the train. The only exception is the "station (1)" section beyond 120 m (see Fig. 17a), which is due to the high directivity of the receive antennas, as explained above, and constitutes a good example of a receive signal degradation due to the significant spread of Doppler shift not caused by a high velocity of the train, but for a specific distribution of the AoA of the received multipath components.

### F. SMALL-SCALE FADING ANALYSIS
Small-scale fading is the change in the received signal power due to the interference caused by the different multi path components [53]. To characterize the small-scale fading we consider the wireless channel response amplitude for a single frequency f_0 (tone). We assume that the statistical distribution of the small-scale fading is the same for all the frequencies around 2.6 GHz within a 10 MHz of bandwidth. Firstly, we can express the time-frequency variant channel response for the ith LTE frame as

$$H_i(t,f) = \mathcal{F}_\tau(\tilde{h}_i(t,\tau))$$
$$= \sum_{l=1}^{M} \tilde{\alpha}_{i,l} \exp\left(j2\pi(\tilde{v}_{i,l}t - f\tilde{\tau}_{i,l})\right), \quad (26)$$

where $\mathcal{F}_\tau(\cdot)$ is the Fourier transform with respect to the delay τ. We define $H(t, f)$ as the channel time-frequency response for the whole subway trajectory, analogously to the the time-varying channel impulse response in (5). Then, the channel response amplitude for a given frequency f_0 is

$$E(t) = |H(t, f_0)|. \qquad (27)$$

To analyze the small-scale fading we first remove the slow fading effects (large-scale fading). This is done by averaging over $E(t)$ using a sliding window. As discussed in [55], it is important to choose the correct window size to characterize the small-scale fading without the influence of the large-scale one. In accordance with the indications in [55]–[58], we select a window length of $30\,\lambda$. Fig. 18 shows the received power for the eNodeB-train and the eNodeB-mobile links. Such received power is calculated as $E^2(t)$. A superimposed black dashed curve shows the large-scale fading obtained by averaging the receive power with the above-mentioned sliding window.
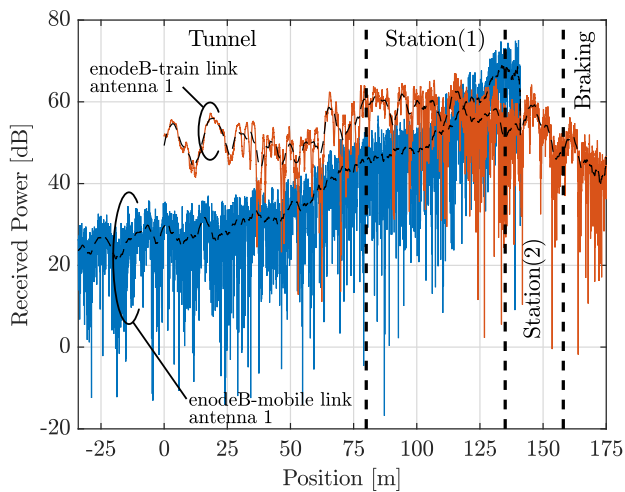
FIGURE 18. Received power for a single frequency $f_0 = 0$ both for eNodeB-train and eNodeB-mobile links. The large-scale fading corresponds to the black dashed curves.

In order to select the best-fitting model for the small-scale fading we use the Akaike's information criteria (AIC) method originally proposed in [59]. Considering a set of models that may fit the data, the AIC method allows us to estimate the goodness of fit for each model. A good explanation on model selection and on the AIC method can be found in [60]. In particular, for selecting the best fitting model for the small-scale fading, the AIC method has been extensively used in the literature [41], [61]–[64]. In this work, we consider the AIC estimator as that derived in [61].

We applied the AIC method to the small-scale fading for both the eNodeB-train and the eNodeB-mobile links. More specifically, we considered 50 samples per meter. The results of the Akaike weights obtained for the different cases are summarized in Table 6.

Figs. 19 and 20 show the small-scale fading CDFs and the distribution fittings for both the eNodeB-train and the

TABLE 6. AIC weights obtained for the small-scale fading.

Antenna	Section	Rician	Rayleigh	Nakagami	Lognormal
mobile 1	Tunnel	1	0	0	0
	Station	0.7709	0.1352	0.0939	0
mobile 2	Tunnel	1	0	0	0
	Station	0.8069	0.1365	0.0566	0
train 1	Tunnel	1	0	0	0
	Station (1)	1	0	0	0
	Station (2)	1	0	0	0
	Braking	0.9999	0	0.0001	0
train 2	Tunnel	1	0	0	0
	Station (1)	1	0	0	0
	Station (2)	0.9991	0	0.0009	0
	Braking	0.9524	0	0.0476	0
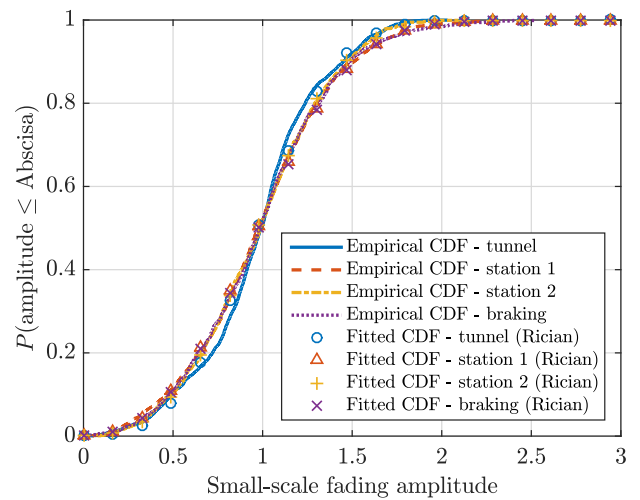
FIGURE 19. CDF and fittings of the small-scale fading for the eNodeB-train link (antenna 1).
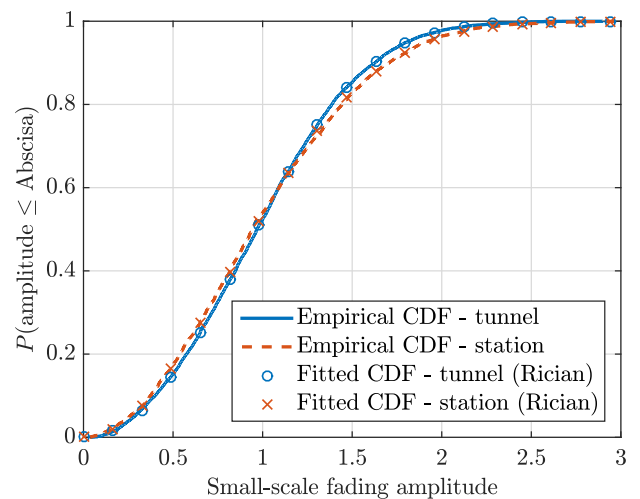
FIGURE 20. CDF and fittings of the small-scale fading for the eNodeB-mobile link (antenna 1).

eNodeB-mobile links. In all cases, the Rician distribution is the most appropriate choice.

It is also interesting to consider the AIC weights for smaller signal sections, hence accounting for variations of the
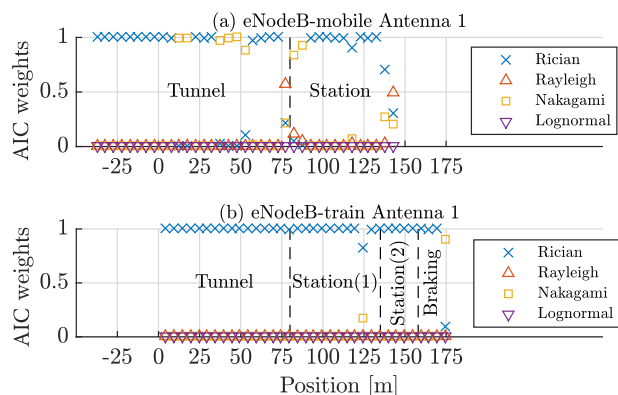
FIGURE 21. AIC weights considering small signal windows.

small-scale parameters for different regions along the train trajectory. Therefore, we also perform the AIC weights estimation considering a window of 15 m with a 5 m step between consecutive estimations. The results obtained are shown in Fig. 21 where, as indicated also in Table 6, the Rician distribution is the best fit. However, for some of the estimated windows, the Nakagami distribution is better. As shown in Fig. 21, this happens for the eNodeB-mobile link during some parts of the ''tunnel'' section and also at the start of the ''station'' section. In such cases, the parameter m of the Nakagami distribution is close to 1 (ranging from 0.96 to 1.15).

G. K-FACTOR ANALYSIS

Fig. 22 shows the K-factor expressed in decibels, obtained for both the train antenna 1 and mobile antenna 1 along the whole train path. The K-factor values shown are computed from the parameters obtained for the Rice distribution fitting carried out to obtain the AIC weights and shown in Fig. 21.
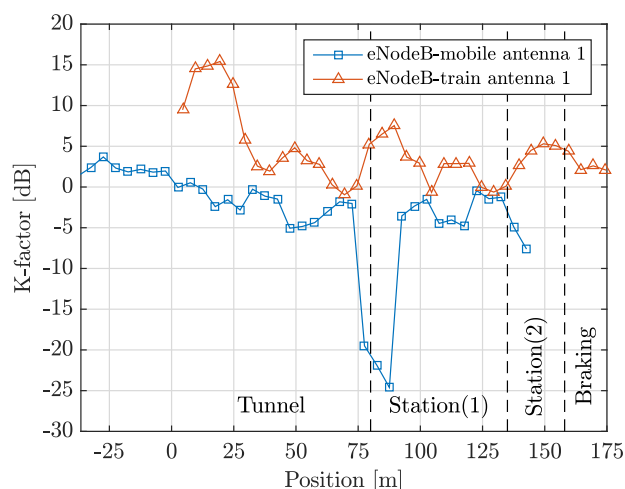

FIGURE 22. K-factor for both the eNodeB-train and the eNodeB-mobile links (antenna 1). Sections for the case of the eNodeB-mobile link are also shown.

In view of the results in Fig. 22, it is clear that the LoS component is almost never received by the mobile antennas

since the K-factor is most of the time below 0 dB. The case of the eNodeB-train link is totally different because a strong LoS component is present during most of the train trajectory, except at those positions where strong reflections are observed, as shown in Fig. 8. Notice that the results in Fig. 22 for the eNodeB-train link are totally consistent with those shown in Fig. 11a for the delay spread, indicating that the dominant path, which is the LoS path in our case, exhibits significantly larger power values than the other paths.

V. CONCLUSIONS

In this work, the wireless channel response of a modern subway station and its corresponding entrance tunnel in the Madrid Metro was characterized in detail. An LTE eNodeB transmitter was setup in the middle of the platform to cyclically transmit standard-compliant FDD LTE signals at a carrier frequency of 2.6 GHz with a bandwidth of 10 MHz. Two receivers were placed in the subway train to investigate both the eNodeB-train and the eNodeB-mobile links. The train was moving at a constant speed of 18 km/h from the entrance tunnel until it is completely stopped at the end of the station. We characterized the wireless channel response for both links based on the following parameters: PDP, RMS delay spread, Doppler PSD, small-scale fading distribution, and K-factor.

The GTEC Testbed in conjunction with the SAGE algorithm revealed themselves as excellent tools to characterize the response of doubly selective wireless channels like those in the considered subway scenario.

The results show that the eNodeB-mobile link, in which the receive antennas are inside the train carriage, is the most challenging one, mainly due to the penetration losses. In addition, the geometry of the station and its entrance tunnel leads to scenarios with very specific propagation properties. More specifically, the RMS delay spread changes significantly from the tunnel to the station. Additionally, the estimated PDPs are consistent with those previously reported in the literature for similar scenarios. It is worth noting that the Doppler effect is actually an aggregation from different contributors, mainly carrier frequency and signal bandwidth, train speed, propagation environment, and the radiation patterns of the transmit and receive antennas. In this case, highly directive receive antennas in the eNodeB-train link block the LoS component at the end of the train trajectory, which leads to a widely-spread Doppler PSD.

The actual Doppler effects present in the receive signal, after correcting the frequency offsets between the transmitter and the receiver, have been also characterized. Assuming an ideal frequency offset estimation and correction and given the low measured speed, it can be concluded that the observed Doppler effects are not very relevant to the receiver if a strong LoS component is present.

Finally, the small-scale fading was characterized. We used the AIC method to find the best fitting distribution for the small-scale fading. We considered four of the

most common distributions used in the literature, namely Rayleigh, Rician, Nakagami, and Lognormal. The analysis revealed that the small-scale fading was best fitted by a Rician distribution for both links (eNodeB-mobile and eNodeB-train), and for the whole train trajectory. The calculated K-Factor values for the eNodeB-mobile link were low (less than 0 dB most of the time). However, K-factor values for the eNodeB-train link exceeded 0 dB most of the time, indicating the presence of a dominant path in the signal.

REFERENCES

[1] S. Schwarz and M. Rupp, "Society in motion: Challenges for LTE and beyond mobile communications," *IEEE Commun. Mag.*, vol. 54, no. 5, pp. 76–83, May 2016.

[2] P. Devaux, *Les chemins de Fer*. Paris, France: Presses universitaires de France, 1943.

[3] J. Alias, *La Voie ferrée: Techniques de Construction et d'Entretien*. Paris, France: Eyrolles, 1984.

[4] S. Chandra and M. M. Agarwal, *Railway Engineering*. Cambridge, U.K.: Cambridge Univ. Press, 1995.

[5] J. R. Piñeiro, "Broadband wireless communication systems for high mobility scenarios," Ph.D. dissertation, Dept. Electron. Syst., Univ. A Coruña, A Coruña, Spain, 2016.

[6] *ETCS/GSM-R Quality of Service–Operational Analysis*, Standard 04E117, eRTMS, 2010.

[7] A. Hrovat, G. Kandus, and T. Javornik, "A survey of radio propagation modeling for tunnels," *IEEE Commun. Surveys Tuts.*, vol. 16, no. 2, pp. 658–669, 2nd Quart., 2014.

[8] K. Guan, Z. Zhong, J. I. Alonso, and C. Briso-Rodríguez, "Measurement of distributed antenna systems at 2.4 GHz in a realistic subway tunnel environment," *IEEE Trans. Veh. Technol.*, vol. 61, no. 2, pp. 834–837, Feb. 2012.

[9] A. E. Forooshani, S. Bashir, D. G. Michelson, and S. Noghanian, "A survey of wireless communications and propagation modeling in underground mines," *IEEE Commun. Surveys Tuts.*, vol. 15, no. 4, pp. 1524–1545, 4th Quart., 2013.

[10] A. V. Popov and N. Y. Zhu, "Modeling radio wave propagation in tunnels with a vectorial parabolic equation," *IEEE Trans. Antennas Propag.*, vol. 48, no. 9, pp. 1403–1412, Sep. 2000.

[11] G. D. Kondylis, F. De Flaviis, G. J. Pottie, and Y. Rahmat-Samii, "Indoor channel characterization for wireless communications using reduced finite difference time domain (R-FDTD)," in *Proc. IEEE VTS 50th Veh. Technol. Conf. (VTC-Fall)*, vol. 3, Sep. 1999, pp. 1402–1406.

[12] M. M. Rana and A. S. Mohan, "Segmented-locally-one-dimensional-FDTD method for EM propagation inside large complex tunnel environments," *IEEE Trans. Magn.*, vol. 48, no. 2, pp. 223–226, Feb. 2012.

[13] P. Bernardi, D. Caratelli, R. Cicchetti, V. Schena, and O. Testa, "A numerical scheme for the solution of the vector parabolic equation governing the radio wave propagation in straight and curved rectangular tunnels," *IEEE Trans. Antennas Propag.*, vol. 57, no. 10, pp. 3249–3257, Oct. 2009.

[14] R. Martelly and R. Janaswamy, "An ADI-PE approach for modeling radio transmission loss in tunnels," *IEEE Trans. Antennas Propag.*, vol. 57, no. 6, pp. 1759–1770, Jun. 2009.

[15] A. Emslie, R. Lagace, and P. Strong, "Theory of the propagation of UHF radio waves in coal mine tunnels," *IEEE Trans. Antennas Propag.*, vol. AP-23, no. 2, pp. 192–205, Mar. 1975.

[16] D. G. Dudley, S. F. Mahmoud, M. Lienard, and P. Degauque, "On wireless communication in tunnels," in *Proc. IEEE Antennas Propag. Soc. Int. Symp.*, Jun. 2007, pp. 3305–3308.

[17] T. Klemenschits and E. Bonek, "Radio coverage of road tunnels at 900 and 1800 MHz by discrete antennas," in *Proc. 5th IEEE Int. Symp. Pers., Indoor Mobile Radio Commun., Wireless Netw.-Catching Mobile Future*, vol. 2, Sep. 1994, pp. 411–415.

[18] Y. P. Zhang, "Novel model for propagation loss prediction in tunnels," *IEEE Trans. Veh. Technol.*, vol. 52, no. 5, pp. 1308–1314, Sep. 2003.

[19] L. Deryck, "Natural propagation of electromagnetic waves in tunnels," *IEEE Trans. Veh. Technol.*, vol. VT-27, no. 3, pp. 145–150, Aug. 1978.

[20] J. R. Wait, "Propagation in rectangular tunnel with imperfectly conducting walls," *Electron. Lett.*, vol. 16, no. 13, pp. 521–522, Jun. 1980.

[21] S.-H. Chen and S.-K. Jeng, "SBR image approach for radio wave propagation in tunnels with and without traffic," *IEEE Trans. Veh. Technol.*, vol. 45, no. 3, pp. 570–578, Aug. 1996.

[22] D. Didascalou, T. M. Schafer, F. Weinmann, and W. Wiesbeck, "Ray-density normalization for ray-optical wave propagation modeling in arbitrarily shaped tunnels," *IEEE Trans. Antennas Propag.*, vol. 48, no. 9, pp. 1316–1325, Sep. 2000.

[23] M. H. Kermani and M. Kamarei, "A ray-tracing method for predicting delay spread in tunnel environments," in *Proc. IEEE Int. Conf. Pers. Wireless Commun.*, Dec. 2000, pp. 538–542.

[24] S. F. Mahmoud and J. R. Wait, "Geometrical optical approach for electromagnetic wave propagation in rectangular mine tunnels," *Radio Sci.*, vol. 9, no. 12, pp. 1147–1158, Dec. 1974.

[25] J.-M. Molina-Garcia-Pardo, J.-V. Rodriguez, and L. Juan-Llácer, "Wideband measurements and characterization at 2.1 GHz while entering in a small tunnel," *IEEE Trans. Veh. Technol.*, vol. 53, no. 6, pp. 1794–1799, Nov. 2004.

[26] E. Masson, P. Combeau, M. Berbineau, R. Vauzelle, and Y. Pousset, "Radio wave propagation in arched cross section tunnels - simulations and measurements," *J. Commun.*, vol. 4, no. 4, pp. 276–283, 2009.

[27] A. Hrovat, G. Kandus, and T. Javornik, "Four-slope channel model for path loss prediction in tunnels at 400 MHz," *IET Microw., Antennas Propag.*, vol. 4, no. 5, pp. 571–582, May 2010.

[28] Y. P. Zhang, G. X. Zheng, and J. H. Sheng, "Radio propagation at 900 MHz in underground coal mines," *IEEE Trans. Antennas Propag.*, vol. 49, no. 5, pp. 757–762, May 2001.

[29] F. M. Pallares, F. J. P. Juan, and L. Juan-Llacer, "Analysis of path loss and delay spread at 900 MHz and 2.1 GHz while entering tunnels," *IEEE Trans. Veh. Technol.*, vol. 50, no. 3, pp. 767–776, May 2001.

[30] M.-S. Choi, D.-Y. Kim, H.-S. Jo, J.-G. Yook, and H.-K. Park, "Path-loss characteristics in subway tunnels at 2.65 GHz," *Microw. Opt. Technol. Lett.*, vol. 48, no. 2, pp. 383–386, 2006.

[31] X. Cai, X. Yin, X. Cheng, and A. P. Yuste, "An empirical random-cluster model for subway channels based on passive measurements in UMTS," *IEEE Trans. Commun.*, vol. 64, no. 8, pp. 3563–3575, Aug. 2016.

[32] L. Zhang *et al.*, "Delay spread and electromagnetic reverberation in subway tunnels and stations," *IEEE Antennas Wireless Propag. Lett.*, vol. 15, pp. 585–588, 2016.

[33] L. Zhang *et al.*, "Experimental evaluation of 4G technologies in metro tunnel scenarios," in *Proc. 10th Eur. Conf. Antennas Propag. (EuCAP)*, Davos, Switzerland, Apr. 2016, pp. 1–5.

[34] T. Domínguez-Bolaño, J. Rodríguez-Piñeiro, J. A. García-Naya, and L. Castedo, "Experimental characterization of LTE wireless links in high-speed trains," *Wireless Commun. Mobile Comput.*, vol. 2017, Sep. 2017, Art. no. 5079130, 10.1155/2017/5079130.

[35] B. H. Fleury, M. Tschudin, R. Heddergott, D. Dahlhaus, and K. I. Pedersen, "Channel parameter estimation in mobile radio environments using the SAGE algorithm," *IEEE J. Sel. Areas Commun.*, vol. 17, no. 3, pp. 434–450, Mar. 1999.

[36] 3GPP, *Technical Specification Group Radio Access Network; Mobile Relay for E-UTRA*, document 3GPP TR 36.836, 2012.

[37] *Technical Specification Group Radio Access Network; Evolved Universal Terrestrial Radio Access (E-UTRA); Physical Channels and Modulation (Release 14)*, document 3GPP TS 36.211 v14.2.0, 2017.

[38] T. Domínguez-Bolaño, J. Rodríguez-Piñeiro, J. A. Garcia-Naya, and L. Castedo, "The GTEC 5G link-level simulator," in *Proc. 1st Int. Workshop Link- Syst. Level Simulations (IWSLS2)*, Vienna, Austria, Jul. 2016, pp. 1–6.

[39] *GTEC Tstbed Project*. Accessed: Sep. 18, 2018. [Online]. Available: https://bitbucket.org/tomas_bolano/gtec_testbed_public.git

[40] P. Suárez-Casal, J. Rodríguez-Piñeiro, J. A. García-Naya, and L. Castedo, "Experimental evaluation of the WiMAX downlink physical layer in high-mobility scenarios," *EURASIP J. Wireless Commun. Netw.*, vol. 2015, no. 109, Dec. 2014.

[41] L. Zhang *et al.*, "Propagation modeling for outdoor-to-indoor and indoor-to-indoor wireless links in high-speed train," *Measurement*, vol. 110, pp. 43–52, Nov. 2017.

[42] T. Domínguez-Bolaño, J. Rodríguez-Pifieiro, J. A. García-Naya, and L. Castedo, "Throughput-based performance evaluation of 5G-candidate waveforms in high speed scenarios," in *Proc. 25th Eur. Signal Process. Conf. (EUSIPCO)*, Kos, Greece, Aug./Sep. 2017, pp. 613–617.

[43] J. Rodríguez-Piñeiro, T. Domínguez-Bolaño, J. A. García-Naya, and L. Castedo, "Performance assessment of 5G-candidate waveforms in high speed scenarios," in *Proc. IEEE 27th Annu. Int. Symp. Pers., Indoor, Mobile Radio Commun. (PIMRC)*, Sep. 2016, pp. 1–6.

[44] D. Fei, J. Rodríguez-Piñeiro, J. A. Garcia-Naya, L. Castedo, K. Guan, and L. Xiong, "TD-LTE downlink performance assessment in high speed scenarios," in *Proc. IEEE 83rd Veh. Technol. Conf. (VTC Spring)*, Nanjing, China, May 2016, pp. 1–5.

[45] J. Rodríguez-Piñeiro, J. A. García-Naya, P. Suárez-Casal, C. Briso-Rodríguez, J. Alonso-Montes, and L. Castedo, "Assessment of channel propagation conditions for FDD LTE transmissions in the spanish high-speed railways," in *Proc. 10th Eur. Conf. Antennas Propag. (EuCAP)*, Davos, Switzerland, Apr. 2016, pp. 1–5.

[46] J. Rodríguez-Piñeiro, T. Domnguez-Bolaño, P. Suárez-Casal, J. A. Garcia-Naya, and L. Castedo, "Affordable evaluation of 5G modulation schemes in high speed train scenarios," in *Proc. 20th Int. ITG Workshop Smart Antennas (WSA)*, Munich, Germany, Mar. 2016, pp. 476–483. [Online]. Available: http://ieeexplore.ieee.org/stamp/stamp.jsp?arnumber=7499166

[47] *Mini-Circuits TVA-11-422*. [Online]. Available: http://www.minicircuits.com/pdfs/TVA-11-422.pdf

[48] *Hyperlink Technologies HG2414P*. [Online]. Available: http://www.l-com.com/multimedia/datasheets/DS_HG2414P.PDF

[49] S. Sesia, I. Toufik, and M. Baker, Eds., *LTE–The UMTS Long Term Evolution: From Theory to Practice*, 2nd ed. Hoboken, NJ, USA: Wiley, 2011.

[50] P. J. Huber, *Robust Statistics*. Hoboken, NJ, USA: Wiley, 1981.

[51] X. Yin, X. Cai, X. Cheng, J. Chen, and M. Tian, "Empirical geometry-based random-cluster model for high-speed-train channels in UMTS networks," *IEEE Trans. Intell. Transp. Syst.*, vol. 16, no. 5, pp. 2850–2861, Oct. 2015.

[52] T. S. Rappaport, *Wireless Communications: Principles and Practice*, vol. 2. Upper Saddle River, NJ, USA: Prentice-Hall, 1996.

[53] A. F. Molisch, *Wireless Communications*, vol. 34. Hoboken, NJ, USA: Wiley, 2012.

[54] A. Meijerink and A. F. Molisch, "On the physical interpretation of the Saleh–Valenzuela model and the definition of its power delay profiles," *IEEE Trans. Antennas Propag.*, vol. 62, no. 9, pp. 4780–4793, Sep. 2014.

[55] R. He, Z. Zhong, B. Ai, G. Wang, J. Ding, and A. F. Molisch, "Measurements and analysis of propagation channels in high-speed railway viaducts," *IEEE Trans. Wireless Commun.*, vol. 12, no. 2, pp. 794–805, Feb. 2013.

[56] W. C. Y. Lee, "Estimate of local average power of a mobile radio signal," *IEEE Trans. Veh. Technol.*, vol. VT-34, no. 1, pp. 22–27, Feb. 1985.

[57] B. Ai, Z. D. Zhong, G. Zhu, and M. Zhao, "Novel statistical criteria for local mean power estimation in wireless coverage prediction," *IET Microw. Antennas Propag.*, vol. 5, no. 5, pp. 596–604, Apr. 2011.

[58] B. Ai, Z. D. Zhong, G. Zhu, and J. P. Liu, "Novel statistical processing methods for wireless field strength prediction," in *Proc. IET Int. Commun. Conf. Wireless Mobile Comput. (CCWMC)*, Dec. 2009, pp. 129–132.

[59] H. Akaike, "A new look at the statistical model identification," *IEEE Trans. Autom. Control*, vol. AC-19, no. 6, pp. 716–723, Dec. 1974.

[60] K. P. Burnham and D. R. Anderson, *Model Selection and Multimodel Inference: A Practical Information-Theoretic Approach*. New York, NY, USA: Springer, 2003.

[61] U. G. Schuster and H. Bolcskei, "Ultrawideband channel modeling on the basis of information-theoretic criteria," *IEEE Trans. Wireless Commun.*, vol. 6, no. 7, pp. 2464–2475, Jul. 2007.

[62] S. Wyne, A. P. Singh, F. Tufvesson, and A. F. Molisch, "A statistical model for indoor office wireless sensor channels," *IEEE Trans. Wireless Commun.*, vol. 8, no. 8, pp. 4154–4164, Aug. 2009.

[63] X. H. Mao, Y. H. Lee, and B. C. Ng, "Statistical modeling of signal variation for propagation along a lift shaft," *IEEE Antennas Wireless Propag. Lett.*, vol. 9, pp. 752–755, 2010.

[64] R. He, B. Ai, Z. Zhong, A. F. Molisch, R. Chen, and Y. Yang, "A measurement-based stochastic model for high-speed railway channels," *IEEE Trans. Intell. Transp. Syst.*, vol. 16, no. 3, pp. 1120–1135, Jun. 2015.

TOMÁS DOMÍNGUEZ-BOLAÑO received the B.S. degree in computer engineering from the University of A Coruña (UDC), A Coruña, Spain, in 2014, where he is currently pursuing the Ph.D. degree. Since 2014, he has been with the Group of Electronics Technology and Communications, UDC. In 2018, he was a Visiting Scholar with Tongji University, Shanghai, China. His research interests include channel measurements, parameter estimation and modeling, and experimental evaluation of wireless communication systems.

JOSÉ RODRÍGUEZ-PIÑEIRO received the B.Sc. degree in telecommunications and the M.Sc. degree in signal processing applications for communications from the University of Vigo, Pontevedra, Spain, in 2009 and 2011, respectively, and the Ph.D. degree (Hons.) from the University of A Coruña (UDC) in 2016. From 2008 to 2011, he was a Researcher with the Department of Signal and Communications, University of Vigo. He has been with the Group of Electronics Technology and Communications, UDC, as a Researcher since 2011 and a Post-Doctoral Researcher since 2017. In 2017, he joined the College of Electronics and Information Engineering, Tongji University, China. Since 2012, he has been collaborating with the Department of Power and Control Systems and the National University of Asunción, Paraguay, in both teaching and research. He is a member of the research team in over 20 research projects funded by public organizations and private companies. He has co-author over 30 papers in peer-reviewed international journals and conferences. He was awarded with six predoctoral, postdoctoral, and research stay grants. His research interests include the experimental evaluation of digital mobile communications, especially for high mobility environments, including terrestrial and aerial vehicular scenarios.

JOSÉ A. GARCÍA-NAYA (S'07–M'10) received the M.Sc. and Ph.D. degrees in computer engineering from the University of A Coruña (UDC), A Coruña, Spain, in 2005 and 2010, respectively. Since 2005, he has been with the Group of Electronics Technology and Communications, UDC, where he is currently an Associate Professor. He has co-author over 90 peer-reviewed papers in journals and conferences. He is a member of the research team in over 40 research projects funded by public organizations and private companies. His research interests include the experimental evaluation of wireless systems in realistic scenarios (indoors, outdoors, high mobility, and railway transportation), signal processing for wireless communications, wireless sensor networks, specially devoted to indoor positioning systems, and time-modulated antenna arrays applied to wireless communication systems.

XUEFENG YIN (S'01–M'06) received the bachelor's degree in optoelectronics engineering from the Huazhong University of Science and Technology, Wuhan, China, in 1995, and the M.Sc. degree in digital communications and the Ph.D. degree in wireless communications from Aalborg University, Aalborg, Denmark, in 2002 and 2006, respectively. From 2006 to 2008, he was an Assistant Professor with Aalborg University. In 2008, he joined the College of Electronics and Information Engineering, Tongji University, Shanghai, China. He became a Full Professor in 2016 and has been the Vice Dean of the college since 2016. He has authored or co-authored over 100 technical papers and co-authored the book *Propagation Channel Characterization, Parameter Estimation, and Modeling for Wireless Communications* (Wiley, 2016). His research interests include high-resolution parameter estimation for propagation channels, measurement-based channel characterization and stochastic modeling for 5G wireless communications, channel simulation based on random graph models, radar signal processing, and target recognition.

LUIS CASTEDO was born in Santiago de Compostela, Spain, in 1966. He received the Ingeniero de Telecomunicación and the Doctor Ingeniero de Telecomunicación degrees from the Polytechnic University of Madrid, Madrid, Spain, in 1990 and 1993, respectively. From 1994 to 2001, he was an Associate Professor with the Department of Electronics and Systems, University of A Coruña, A Coruña, Spain, where he is currently a Full Professor. He was the Chairman of the Department from 2003 to 2009. He is a Principal Researcher of over 30 research projects funded by public organizations and private companies. He has co-author over 100 papers in peer-reviewed international journals and conferences. His research interests include signal processing and digital communications with special emphasis on blind adaptive filtering, estimation/equalization of multiple-input multiple-output channels, space–time coding, and prototyping of digital communication equipment.

• • •